energies

MDPI

Article

Improved Self-Sensing Speed Control of IPMSM Drive Based on Cascaded Nonlinear Control

Muhammad Usama and Jaehong Kim *

Department of Electrical Engineering, Chosun University, 309, Pilmun-daero, Dong-gu, Gwangju 61452, Korea; osama1199@chosun.kr

* Correspondence: jaehong@chosun.ac.kr; Tel.: +82-10-8220-5665

Abstract: This paper presents a nonlinear cascaded control design that has been developed to (1) improve the self-sensing speed control performance of an interior permanent magnet synchronous motor (IPMSM) drive by reducing its speed and torque ripples and its phase current harmonic distortion and (2) attain the maximum torque while utilizing the minimum drive current. The nonlinear cascaded control system consists of two nonlinear controls for the speed and current control loop. A fuzzy logic controller (FLC) is employed for the outer speed control loop to regulate the rotor shaft speed. Model predictive current control (MPCC) is utilized for the inner current control loop to regulate the drive phase currents. The nonlinear equation for the dq reference current is derived to implement the maximum torque per armature (MTPA) control to achieve the maximum torque while using the minimum current values. The model reference adaptive system (MRAS) was employed for the speed self-sensing mechanism. The self-sensing speed control performance of the IPMSM motor drive was compared with that of the traditional cascaded control schemes. The stability of the sensorless mechanism was studied using the pole placement method. The proposed nonlinear cascaded control was verified based on the simulation results. The robustness of the control design was ensured under various loads and in a wide speed range. The dynamic performance of the motor drive is improved while circumventing the need to tune the proportional-integral (PI) controller. The self-sensing speed control performance of the IPMSM drive was enhanced significantly by the designed cascaded control model.

Keywords: self-sensing speed control; maximum torque per ampere (MTPA); fuzzy logic control (FLC); model predictive current control (MPCC); interior permanent magent synchronous motor (IPMSM); model reference adaptive system (MRAS)

check for updates

Citation: Usama, M.; Kim, J. Improved Self-Sensing Speed Control of IPMSM Drive Based on Cascaded Nonlinear Control. *Energies* **2021**, *14*, 2205. https://doi.org/10.3390/en14082205

Academic Editor: Ricardo J. Bessa

Received: 22 February 2021
Accepted: 9 April 2021
Published: 15 April 2021

Publisher's Note: MDPI stays neutral with regard to jurisdictional claims in published maps and institutional affiliations.

Copyright: © 2021 by the authors. Licensee MDPI, Basel, Switzerland. This article is an open access article distributed under the terms and conditions of the Creative Commons Attribution (CC BY) license (https://creativecommons.org/licenses/by/4.0/).

1. Introduction

Interior permanent magnet synchronous motor (IPMSM) drives are gaining significant attention as variable speed drives in industrial applications. This is because IPMSMs display high efficiency, high power density, low volume, and fast dynamics, and incur low maintenance cost. The replacement of rotor windings with a permanent magnet helps achieve rapid response owing to the low inertia. A permanent magnet produces high magnetic fields, which helps reduce the drive size [1]. Various control techniques are utilized for achieving high control performance (such as cascaded linear control based on vector control and direct torque control) under varying model parameters and external disturbances [2].

A vector control method is one of the traditional control methods employed for controlling IPMSM drives. Vector control typically has a linear cascaded control structure with an outer proportional-integral (PI) speed control loop and inner PI current control loop. The PI controller is the most popular and widely employed controller in the industry because of its simple implementation. However, the nonlinear model of an IPMSM PI controller is sensitive to load disturbance or parametric variations. These issues affect the control design of IPMSM drives for high performance applications [3–5].

With the advancement in semiconductor technology, different nonlinear control structures are being studied for PMSM drives. Most of the nonlinear controllers are designed for the speed control loop. In contrast, the linear PI controller is employed for the current control loop. A sliding mode (SM)) control was designed in [6,7] for the speed loop. This illustrates the robustness of the PMSM drive against parametric variations. Furthermore, it eliminates the chattering problem in the conventional SM control design, which reduces the motor performance. However, these methods are highly dependent on the sliding surface. In [8], closed-loop adaptive control was employed for the PMSM drive control. The advantage of adaptive control is apparent when the recursive least square (RLC) algorithm is utilized for parameter estimation. However, RLC affects the CPU performance, wherein it causes the response of the drive system to slow down owing to the existing differential expression. The online identification of load inertia by utilizing the adaptive control technique was proposed in [9]. A fuzzy inference-based control structure was designed to automatically tune the gain value based on the identified inertia. Artificial intelligence-based control methods such as neural network control (NNC) are recommended in [10]. This displays the advantages of online data training. The NNC is capable of handling nonlinearities more efficiently. However, their application is limited because of many issues such as computational complexity, selection of an effective neural network structure, training of the network, and stability issues of the control design [11].

Model predictive control has emerged as an efficient control technique for power electronics applications [12–14]. Several predictive control techniques have been studied [15–18]. One of the advantages of the model predictive control technique is that it can handle the nonlinearities of multiple outputs and inputs of a plant and execute them in a unified manner. It eliminates the modulation block from the control design and is highly suitable for online optimization [19]. A robust nonlinear cascaded control structure based on model predictive control (MPC) was proposed in [20]. In [21], an optimal predictive controller for continuous time-varying systems was proposed. Nonlinear predictive control for single-input single-output (SISO) and multi-input multi-output (MIMO) systems were proposed in [22,23].

The self-sensing speed control method utilizing the model reference adaptive system (MRAS) was introduced in [24–28]. In [24], the rotor angular velocity was estimated based on the reactive power. This method is less sensitive to parametric variations. The motor parameters of most observer designs are temperature dependent. Ref. [25] introduced an online parameter identification method to overcome these problems. MRAS-based sensorless speed control algorithms that utilize the armature current were employed for a surface-mounted permanent magnet synchronous motor (SM-PMSM) [26–28].

This paper introduces a nonlinear cascaded control structure subjected to load torque as a disturbance. The control structure consists of two control loops: (1) The inner control loop is designed by employing a nonlinear model predictive current control. It regulates the motor phase current by influencing the stator voltage. (2) The outer control loop was designed based on a fuzzy logic controller (an intelligent controller). It can handle disturbances and parametric uncertainties. The output of the speed control loop is the magnitude of the torque T_e that is fed to the maximum torque per armature (MTPA) to obtain i_{dq} reference currents. For the sensorless control mechanism, the adaptive control scheme-based MRAS is employed for the salient PMSM. It has a more complex structure than that previously studied for non-salient PMSMs. The stability of the sensorless control design was verified using the pole placement method. In addition, the adaptive rule for speed estimation is obtained according to Popov's integral inequality.

This paper aims to present the remarkable standstill and vigorous performance of an IPMSM under variable load conditions. We observe that compared with previously designed sensorless control based on the MRAS with cascaded linear or eliminating linear control structure, the proposed nonlinear cascaded control structure shows good performance in terms of convergence rate, drive speed or torque ripples, overshoot, current utilization for the MTPA, and handling of non-linearities. The paper is structured as follows:

The nonlinear modeling of an IPMSM drive and the simplified MTPA control technique are discussed in Section 2. The nonlinear cascaded control structure, conventional methods, and self-sensing speed control with stability analysis are described in Section 3. The simulation results and a comparison with traditional techniques are presented in Section 4 to verify the overall effectiveness of the control model. Finally, Section 5 concludes the paper.

2. Nonlinear Modeling of IPMSM

2.1. IPMSM Dynamic Model

In this study, the IPMSM drive is considered after omitting hysteresis losses, eddy losses, and without saturation. To analyze the dynamic performance of the IPMSM, the mathematical model in the synchronous reference frame is derived as follows [1]:

$$\begin{bmatrix} v_d^e \\ v_q^e \end{bmatrix} = \begin{bmatrix} r_s + L_d p & -\omega_r L_q \\ \omega_r L_d & r_s + L_q p \end{bmatrix} \begin{bmatrix} i_d^e \\ i_q^e \end{bmatrix} + \begin{bmatrix} 0 \\ \omega_r \lambda_m \end{bmatrix}. \tag{1}$$

Here, v_{dq}^e represents the component of the state voltage and i_{dq}^e represents the components of the stator current. The stator resistance is denoted as r_s. In the IPMSM, the stator inductance varies depending on the position of the rotor shaft. This implies that the air gap along the rotor circumference in the IPMSM is variable. Therefore, L_{dq} represents the stator inductance component. The rotor flux linkage and rotor shaft speed are denoted as λ_m and ω_r, respectively. The IPMSM synchronous model with the current variable is expressed as [27]:

$$\frac{d}{dt}\begin{bmatrix} i_d^e \\ i_q^e \end{bmatrix} = \begin{bmatrix} -\frac{r_s}{L_d} & \omega_r \frac{L_q}{L_d} \\ -\omega_r \frac{L_d}{L_q} & -\frac{r_s}{L_q} \end{bmatrix} \begin{bmatrix} i_d^e \\ i_q^e \end{bmatrix} + \begin{bmatrix} \frac{1}{L_d} & 0 \\ 0 & \frac{1}{L_q} \end{bmatrix} \begin{bmatrix} v_d^e \\ v_q^e \end{bmatrix} + \begin{bmatrix} 0 \\ -\frac{\lambda_m \omega_r}{L_q} \end{bmatrix}. \tag{2}$$

The nonlinear characteristic of the torque expression in the synchronous reference frame for the IPMSM drive is expressed [1]:

$$T_e = \frac{3P}{2}[\lambda_m i_q^e + (L_d - L_q) i_d^e i_q^e]. \tag{3}$$

The mechanical model of the IPMSM drive in the synchronous reference frame is expressed as

$$\frac{d\omega_m}{dt} = \frac{3P}{2J}[\lambda_m i_q^e + (L_d - L_q) i_d^e i_q^e] - \frac{B}{J}\omega_m - \frac{T_L}{J}. \tag{4}$$

The first term on the right-hand side is the summation of the magnetic and reluctance torques. The pole pair is represented by P, ω_m is the mechanical shaft speed, T_L is the drive load torque torque (the unknown external disturbance), and J and B are the inertia and damping coefficient, respectively, of the rotor.

In IPMSM drives, the variations in inductance depend on the rotor angle because of the magnetic saliency. If the q-axis current control scheme is considered, at steady state, the torque is directly proportional to the q-axis reference current. However, the reluctance torque is not fully utilized. Different MTPA control schemes for increasing the drive efficiency are discussed in the literature. The symbol $*$ in the superscript represents the reference signal. In [29], the MTPA control scheme was introduced by i_d^* and i_q^* as:

$$i_d^* = \frac{\lambda_m}{2(L_q - L_d)} - \sqrt{\frac{\lambda_m^2}{4(L_q - L_d)^2} + i_q^{*2}}. \tag{5}$$

Ref. [30] expressed the control law by the magnitude of the stator current vector I_s and the current angle β given as:

$$\beta = \sin^{-1}\left[\frac{\lambda_m - \sqrt{\lambda_m^2 + 8[L_q - L_d]^2 I_s^2}}{4[L_q - L_d] I_s}\right]. \tag{6}$$

Equation (6) can be simplified to express the control law in terms of i_d^* and I_s, as follows:

$$i_d^* = \frac{\lambda_m - \sqrt{\lambda_m^2 + 8[L_q - L_d]^2 I_s^2}}{4[L_q - L_d]}. \tag{7}$$

As mentioned above, control laws are widely employed in MTPA operations. For simplicity, (5) is expanded by Taylor series expansion across the zero point [31]. Higher-order terms are omitted because their contributions are negligible. These are expressed as

$$i_d^* = \frac{[L_d - L_q]}{\lambda_m} i_q^{*2}. \tag{8}$$

For i_q^*, (5) is solved using the motor control parameters given in Table 1 to yield

$$i_d^* = 16.72 - \sqrt{279.62 + i_q^{*2}}. \tag{9}$$

Equation (9) is expanded by the Taylor series expansion at $i_q^* = 0.001$. By omitting the smaller terms,

$$i_d^* = -0.0299(i_q^* - 0.001)^2. \tag{10}$$

Substituting (10) into (3) with the given motor parameters and solving for the i_q^* yield,

$$i_q^* = 0.437T_e + 0.001. \tag{11}$$

The current online reference for the MTPA operation is obtained by employing (8) and (11).

Table 1. Simulation Parameters.

Parameters	Symbols	Values
Sampling Time	T_s	1 µs
DC-link	V_{dc}	500 V
Stator resistance	r_s	2.5 Ω
Pole pairs	P	3
d-axis Inductance	L_d	15.025 mH
q-axis Inductance	L_q	30.175 mH
Moment of inertia	J	0.00365 kgm^2
Flux	λ_m	0.5283 Wb
Damping coefficient	B	0.0011 Nm·s

2.2. VSI Fed IPMSM

A two-level three-phase voltage source inverter (2L3P-VSI) was employed in this study. The VSI connected to the IPMSM drive is shown in Figure 1. The DC voltage source is the input to the VSI, and each armature phase of the motor is connected to each leg of a three-phase inverter. The operation of the two switches in each inverter phase is nonsimultaneous. This is to prevent short-circuiting of the input voltage source. The IGBT switches provide the voltage across the motor drive based on the switching signal provided by the control design. The switching state of the inverter for each phase is expressed as (12). Eight switching configurations were applied across the VSI (two inactive base voltage vectors and six active voltage vectors). Table 2 lists the corresponding voltage vectors for each switching state. A set of seven switching configurations was obtained in the complex plane as $v_0 = v_7$ [32]:

$$S = \frac{2}{3}(S_1 + e^{j\frac{2\pi}{3}} S_3 + e^{-j\frac{2\pi}{3}} S_5). \tag{12}$$

The feasible output voltage vector generated by the VSI is obtained from (12) as

$$V_i = V_{dc} S, \tag{13}$$

where i represents seven switching configurations.

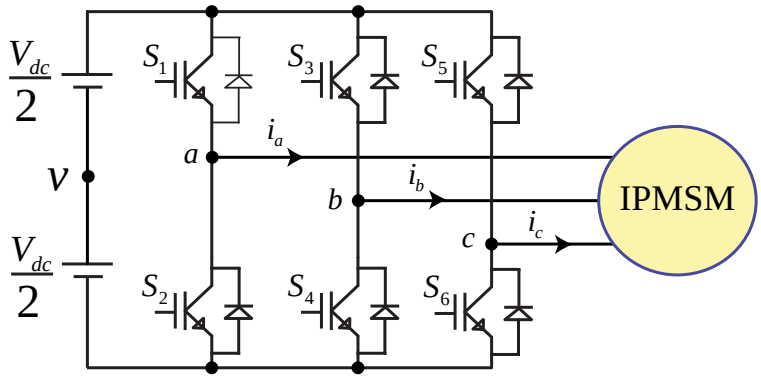


Figure 1. VSI fed IPMSM.

Table 2. Switching states and voltage vector applied across VSI.

Inverter on Legs	Voltage Vector	Switching States		
		S_1	S_3	S_5
S_2, S_4, S_6	$v_0 = 0$	0	0	0
S_2, S_4, S_5	$v_1 = -\frac{1}{3}V_{dc} - j\frac{\sqrt{3}}{3}V_{dc}$	0	0	1
S_2, S_3, S_6	$v_2 = -\frac{1}{3}V_{dc} + j\frac{\sqrt{3}}{3}V_{dc}$	0	1	0
S_2, S_3, S_5	$v_3 = -\frac{2}{3}V_{dc}$	0	1	1
S_1, S_4, S_6	$v_4 = \frac{2}{3}V_{dc}$	1	0	0
S_1, S_4, S_5	$v_5 = \frac{1}{3}V_{dc} - j\frac{\sqrt{3}}{3}V_{dc}$	1	0	1
S_1, S_3, S_6	$v_6 = \frac{1}{3}V_{dc} + j\frac{\sqrt{3}}{3}V_{dc}$	1	1	0
S_1, S_3, S_5	$v_7 = 0$	1	1	1

3. Control Strategies

This section describes the proposed control strategy for an IPMSM drive. It has two main stages, which are discussed comprehensively in this section. A nonlinear cascaded control structure is described in the first part, and the sensorless mechanism and stability analysis are described.

3.1. Nonlinear Cascaded Control Structure

This section first describes the external automatic speed control loop designed based on a fuzzy logic controller (FLC). The inner current control loop, which is modeled based on predictive control, is discussed in detail. Furthermore, a convergence analysis of an inner current control loop is presented briefly.

3.1.1. Intelligent Speed Control Loop

In this study, an external control model was designed by employing the FLC. It is a highly convenient and effective means to draw a definitive conclusion based on unclear, imprecise, ambiguous, or incomplete input data. The FLC was employed to achieve the maximum torque sensitivity of the motor drive. Because of the nonlinear characteristic of torque expression, complexity emerges as the electrical components undergo significant perturbation under various steady-state and transient load conditions. Because the FLC is capable of handling the nonlinearity in the system, the load can be considered as a nonlinear mechanical characteristic and modeled by the following expression [33]:

$$T_L = A\omega_m^2 + B\omega_m + C, \tag{14}$$

where A, B, and C are arbitrary constant. Substituting (14) into (4), we obtain

$$J_m\dot{\omega}_m = T_e - (B + B_m)\omega_m - A\omega_m^2 - C. \tag{15}$$

A marginal variation in the electrical torque of the motor would cause the motor speed to vary. Therefore, Equation (15) can be expressed as [34]:

$$J_m \Delta\dot{\omega}_m = \Delta T_e - (B + B_m)\Delta\omega_m - A\Delta\omega_m^2. \tag{16}$$

The continuous terms in (16) are replaced by their finite differences. The discrete-time small-signal model of the motor drive with a nonlinear load is expressed as [33,34]:

$$T_e(n) = \int_{discrete} \Delta T_e(n) = f(\Delta e(n), \Delta\omega_m(n)), \tag{17}$$

where $\Delta e(n)$represents the variation in speed error between the present and past samples at the sampling time t_s, $\Delta\omega_m(n)$ represents the variation in the estimated and reference speeds of the drive during the sampling period t_s, f represents the nonlinear function. The nonlinear relationship between the drive speed and torque was mapped using the FLC. The reference currents required to generate the desired motor speed are obtained from (8), (11), and (17).

A structural diagram of the FLC incorporating the MTPA control technique is shown in Figure 2.

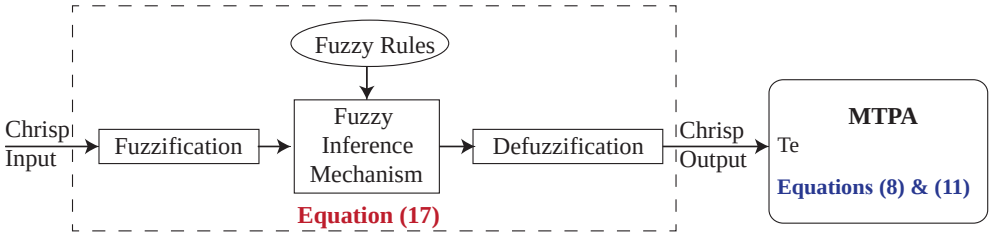


Figure 2. Fuzzy logic control for speed regulator.

In this study, a trapezoidal membership function was used as the upper and lower bounds, whereas the triangular membership function was used to represent the mid values in the input space. Both functions are convenient to implement and do not have a complex mathematical model. This would help reduce the computational complexity. Trapezoidal functions are used for the negative high (NH) and positive high (PH) functions for all input and output vectors. In contrast, the triangular membership function is employed for the negative medium (NM), negative low (NL), zero (ZE), positive medium (PM), and positive low (PL). The triangular and trapezoidal membership functions of the fuzzy system are expressed as [35]

$$\mu_{F(x)} = \begin{cases} 0, & x < a \\ \frac{x-a}{b-x}, & a \le x < b \\ \frac{c-x}{c-b}, & b \le x \le c \\ 0, & x > c \end{cases} \tag{18}$$

and

$$\mu_{F(x)} = \begin{cases} 0, & x < a \\ \frac{b-a}{b-x}, & a \le x < b \\ \frac{d-x}{d-c}, & c \le x < d \\ 0, & x > d \end{cases} \tag{19}$$

The parameters $[a, b, c, d]$ define the membership functions that specify the axis coordinates. In this study, the Mamdani-type fuzzy inference mechanism was utilized [36]. Furthermore, the values for the membership functions and fuzzy rules are set based on the trial-and-error approach to ensure optimal performance of the motor drive. Table 3 lists the rules of the fuzzy controller. In total, 49 rules were established based on the input signals, $\Delta e(n)$ and $\Delta\omega_m(n)$. The following rules describe the working mechanism of the FLC:

a If $\Delta\omega_m(n)$ and $\Delta e(n)$ are NH, then the value across the output is NH.

b If $\Delta\omega_m(n)$ and $\Delta e(n)$ are NH and PH, respectively, then the value across the output is ZE.

c If $\Delta\omega_m(n)$ and $\Delta e(n)$ are PH and ZE,respectively, then the value across the output is PH.
d If $\Delta\omega_m(n)$ and $\Delta e(n)$ are ZE and NH, respectively, then the value across the output is NH.

Table 3. Fuzzy rules for fuzzy inference mechanism.

$\downarrow \Delta\omega_m \setminus \Delta e \rightarrow$	**NH**	**NM**	**NL**	**ZE**	**PL**	**PM**	**PH**
NH	NH	NH	NH	NH	NM	NL	ZE
NM	NH	NH	NH	NM	NL	ZE	PL
NL	NH	NH	NM	NL	ZE	PL	PM
ZE	NH	NM	NL	ZE	PL	PM	PH
PL	NL	NL	ZE	PL	PM	PH	PH
PM	NL	ZE	PL	PM	PH	PH	PH
PH	ZE	PL	PM	PH	PH	PH	PH

3.1.2. Finite Set Current Predictive Control of IPMSM

Finite set current predictive control (FSCPC) is a model-based nonlinear control that is simple and convenient to implement. The objective of the controller is to regulate the output control variable in conjunction with reference values by controlling the inverter switches. The main concept is to employ the system's model to predict the future response until the horizon time and to determine the decision function that shows the desired response of the system. Optimal results are obtained by lowering the cost index function.

The FSCPC employs the discrete-time model of the IPMSM to predict the future output control variable in conjunction with its reference trajectories at each sampling time frame T_s. The discrete-time model of the IPMSM has the form of

$$\begin{aligned} x^{k+1} &= A_d x^k + B_d u^k \\ y^k &= C_d x^k + D_d u^k \end{aligned} \tag{20}$$

The three-phase voltage of the two-level VSI is determined from (12) and (13) and transformed into the dq voltage by employing Park's transformation [27].

$$\begin{bmatrix} v_{as} \\ v_{bs} \\ v_{cs} \end{bmatrix} = \frac{V_{dc}}{3} \begin{bmatrix} 2 & -1 & -1 \\ -1 & 2 & -1 \\ -1 & -1 & 2 \end{bmatrix} \begin{bmatrix} S_1 \\ S_3 \\ S_5 \end{bmatrix}, \tag{21}$$

and

$$\begin{bmatrix} v_d^e \\ v_q^e \\ v_0^e \end{bmatrix} = \frac{2}{3} \begin{bmatrix} cos\theta & cos(\theta - \frac{2\pi}{3}) & cos(\theta + \frac{2\pi}{3}) \\ -sin\theta & -sin(\theta - \frac{2\pi}{3}) & -sin(\theta + \frac{2\pi}{3}) \\ \frac{1}{\sqrt{2}} & \frac{1}{\sqrt{2}} & \frac{1}{\sqrt{2}} \end{bmatrix} \begin{bmatrix} v_{as} \\ v_{bs} \\ v_{cs} \end{bmatrix}. \tag{22}$$

Thus, the discretization of the system input and output vectors utilizing the inverter model based on the forward Euler approximation is derived as follows:

$$\begin{aligned} v_d^k &= r_s i_d^k + \frac{L_d}{T_s}(i_d^{k+1} - i_d^k) - \omega_r^k L_q i_q^k, \\ v_q^k &= r_s i_q^k + \frac{L_q}{T_s}(i_q^{k+1} - i_q^k) + \omega_r^k L_d i_d^k + \omega_r^k \lambda_m. \end{aligned} \tag{23}$$

Therefore, the discrete-time model of the drive for the output control vector is obtained using (23) and is expressed as

$$\begin{aligned} i_d^{k+1} &= [(1 - \frac{T_s r_s}{L_d}) i_d^k + \frac{T_s}{L_d}(\omega_r^k L_q i_q^k + v_d^k)], \\ i_q^{k+1} &= [(1 - \frac{T_s r_s}{L_q}) i_q^k + \frac{T_s}{L_q}(v_q^k - \omega_r^k L_d i_q^k - \omega_r^k \lambda_m)]. \end{aligned} \tag{24}$$

The FSCPC employs the discrete-time model of the IPMSM drive to predict the behavior of the output control vector for each switching state. Selection of the decision or cost function is significant because the optimal voltage vector is applied to the drive based on the minimization of the predefined cost function. The cost function was selected to attain the minimum error between the reference and predictive output currents as

$$h = (i_d^{*k} - i_d^{k+1})^2 + (i_q^{*k} - i_q^{k+1})^2. \tag{25}$$

The optimal voltage vectors applied across the IPMSM were selected based on (25). The optimal voltage vectors based on the switching states presented in Table 2 are fed to the inverter. In addition, the applied drive phase currents are compelled to converge to the reference phase currents obtained from the external speed loop by incorporating the MTPA algorithm in the next sampling period. This results in the application of the predictive current across the motor drive and the operation of the motor drive based on the reference current trajectories.

A schematic diagram of the FSCPC consisting of a one-step horizon for the two-level three-phase VSI-fed IPMSM drive is shown in Figure 3.

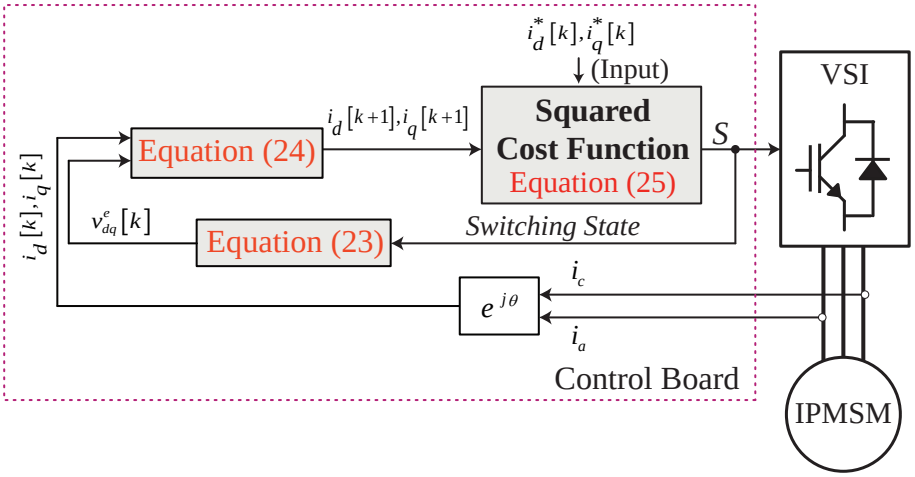


Figure 3. Structural diagram of FSCPC for three-phase VSI fed IPMSM.

Convergence Analysis

To perform a stability analysis of the current predictive control, we consider a positive real function V^k [37]:

$$V^k \equiv |e_d^k|^2 + |e_q^k|^2, \tag{26}$$

where $e_d^k = i_d^{*k} - i_d^k$ and $e_q^k = i_q^{*k} - i_q^k$. The current reference can be fixed with a sufficiently large sampling frequency in the steady state, that is, $i_d^{*k+1} = i_d^{*k}$. Therefore, the d-axis current error at the $(k+1)$th sampling instant is calculated using (24) as

$$e_d^{k+1} = i_d^{*k} - i_d^{k+1} = e_d^k + \underbrace{\frac{T_s}{L_d}\left(r_s i_d^k - \omega_r^k L_q i_q^k - v_d^k\right)}_{u_d^k}.$$

Then it is evident from Minkowski's inequality that

$$|e_d^{k+1}|^2 = |e_d^k + u_d^k|^2 \leq |e_d^k|^2 + |u_d^k|^2,$$

for all u_d^k values. By substituting u_d^k into (23), we obtain $u_d^k = i_d^k - i_d^{k+1}$. In addition, the volt-second balance condition at the stator inductance, L_d, during the steady state implies that $i_d^k - i_d^{k+1} = 0$. Therefore, the following inequality holds:

$$|e_d^{k+1}|^2 - |e_d^k|^2 \leq 0. \tag{27}$$

A monotonic decrease in $|e_d^k|^2$ is achieved with this negative squared error difference.

Meanwhile, the q-axis current error, e_q^{k+1}, is calculated using (24) with a fixed current reference as

$$e_q^{k+1} = i_q^{*k} - i_q^{k+1} = e_q^k + \underbrace{\frac{T_s}{L_q}\left(r_s i_q^k + \omega_r^k L_d i_d^k + \omega_r^k \lambda_m - v_q^k\right)}_{u_q^k}.$$

Similarly, we can demonstrate that

$$|e_q^{k+1}|^2 - |e_q^k|^2 \leq 0. \tag{28}$$

Hence, $|e_q^k|^2$ also decreases monotonically. As a result, Equation (26), which is of the same form as the specified cost function, monotonically decreases over time. Thus, the proposed system is asymptotically stable.

3.2. Self-Sensing Speed Mechanism

The self-sensing speed control technique for estimating the angular velocity and angle of the rotor is challenging. Various self-sensing speed control methods for motor drives have been discussed in the literature. The closed-loop adaptive control techniques, such as SMO and EKF, yielded erroneous results at low speed and reduced robustness during standstill speed operation. Therefore, an MRAS adaptive control technique that is in accordance with Popov's stability criterion is designed to estimate the output state variable i_{dq} and the angular velocity and position of the rotor. The MRAS is a model-dependent technique. Therefore, the critical step for speed observer design is the selection of a suitable model of the IPMSM drive that reveals algebraic constraints. The MRAS design consists of two models: (1) the reference model that determines the required states, and (2) the adjustable model, which determines the state's estimated values. The two models are then compared. Then, their error signal is fed to an adaptive rule that is designed based on Popov's integral inequality to tune the adjustable model by estimating the shaft speed. MRAS is convenient to execute and can reduce computational complexity. Figure 4 shows a structural diagram of the MRAS-based self-sensing speed estimator scheme. The estimated rotor angular speed tracks the real rotor shaft speed based on an adaptive rule utilizing Popov's theorem. The angular position of the rotor is obtained by integrating the estimated angular velocity.

$$\frac{d}{dt}\begin{bmatrix} \hat{i}_d^e \\ \hat{i}_q^e \end{bmatrix} = \begin{bmatrix} -\frac{r_s}{L_d} & \hat{\omega}_r \frac{L_q}{L_d} \\ -\hat{\omega}_r \frac{L_d}{L_q} & -\frac{r_s}{L_q} \end{bmatrix} \begin{bmatrix} \hat{i}_d^e \\ \hat{i}_q^e \end{bmatrix} + \begin{bmatrix} \frac{1}{L_d} & 0 \\ 0 & \frac{1}{L_q} \end{bmatrix} \begin{bmatrix} v_d^e \\ v_q^e \end{bmatrix} + \begin{bmatrix} 0 \\ -\frac{\lambda_m \hat{\omega}_r}{L_q} \end{bmatrix}. \tag{29}$$

The mathematical model of the IPMSM drive contains information on rotor angular speed, as illustrated in (29). It is used as an adjustable model, whereas the current model of the IPMSM in the synchronous reference frame (2) is considered as the reference model. The symbol $\wedge$ indicates the estimated value of the variables.

To converge the output error between the models to zero, the adaptive rule is developed by employing the error signal from the MRAS self-sensing control scheme. The error equation is derived by subtracting (2) and (29) and is expressed as

$$\frac{d}{dt}e_d = -\frac{r_s}{L_d}e_d + \hat{\omega}_r \frac{L_q}{L_d}e_q + \Delta\omega_r \frac{L_q}{L_d} i_q, \tag{30}$$

$$\frac{d}{dt}e_q = -\frac{r_s}{L_q}e_q - \hat{\omega}_r \frac{L_d}{L_q}e_d - \Delta\omega_r [\frac{L_d}{L_q} i_d + \frac{\lambda_m}{L_q}], \tag{31}$$

and

$$\frac{d}{dt}\begin{bmatrix} e_d \\ e_q \end{bmatrix} = \begin{bmatrix} -\frac{r_s}{L_d} & \hat{\omega}_r \frac{L_q}{L_d} \\ -\hat{\omega}_r \frac{L_d}{L_q} & -\frac{r_s}{L_q} \end{bmatrix} \begin{bmatrix} e_d \\ e_q \end{bmatrix} + \Delta\omega_r \begin{bmatrix} i_q \frac{L_q}{L_d} \\ -i_d \frac{L_d}{L_q} - \frac{\lambda_m}{L_q} \end{bmatrix}. \tag{32}$$

The state error model of the IPMSM drive is obtained as

$$\frac{d}{dt} e_{dq} = \mathbf{A}e + \mathbf{W}. \tag{33}$$

where e is the state error vector $[e_{dq}]^T = [e_d\ e_q]^T$, and $\mathbf{A}$ is the system matrix. $\mathbf{W}$ is the output feedback loop vector and is expressed as follows:

$$\mathbf{A} = \begin{bmatrix} -\frac{r_s}{L_d} & \hat{\omega}_r \frac{L_q}{L_d} \\ -\hat{\omega}_r \frac{L_d}{L_q} & -\frac{r_s}{L_q} \end{bmatrix}, \mathbf{W} = \begin{bmatrix} i_q \frac{L_q}{L_d} \\ -i_d \frac{L_d}{L_q} - \frac{\lambda_m}{L_q} \end{bmatrix} \Delta\omega_r.$$

To ensure drive stability, the MRAC system is remodeled as a nonlinear time-varying feedback system comprising a nonlinear feedback system and a linear feed-forward system. The adaptive system is transformed into an identical model, as shown in Figure 5.

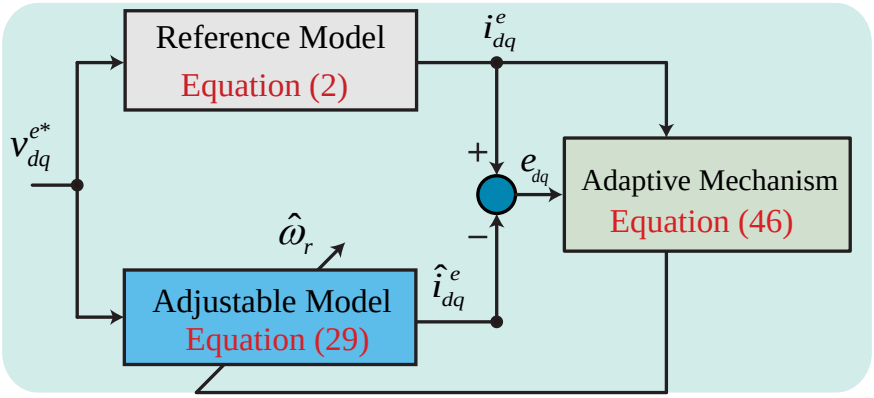


Figure 4. Structural diagram of IPMSM speed self-sensing based on adaptive control.

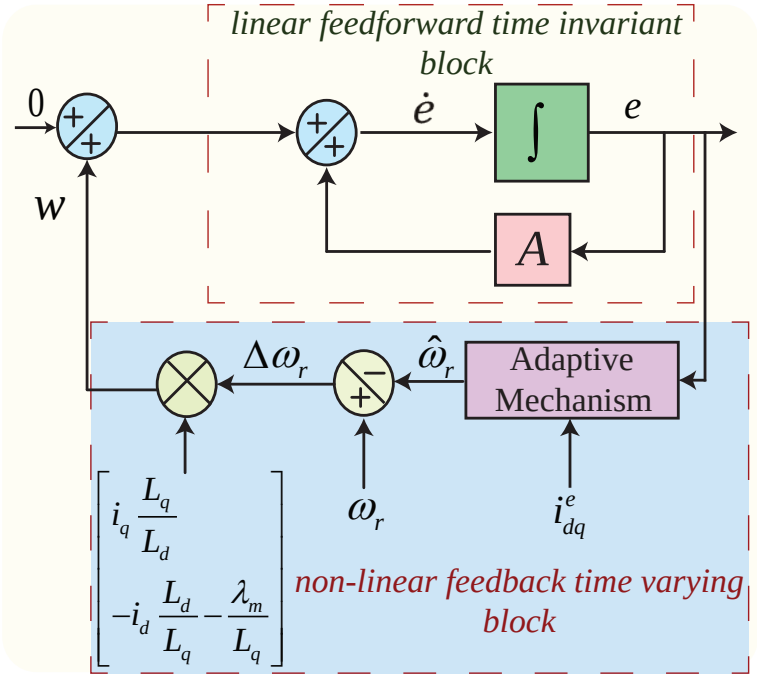


Figure 5. Equivalent model for self-sensing speed estimator.

The adaptive mechanism is designed such that the nonlinear feedback system satisfies Popov's integral inequality [38]. These two norms should be verified to ensure system control stability. First, the linear feed-forward transfer function $G(s)$=$[Is - A]^{-1}$ should be positive real, such that all the poles of the system are located on the left-hand side of the s-plane. The numerical proof for a linear model to be positive real is provided in [27]. The poles of $G(s)$ for the estimated rotor shaft speed ranging from -1200 to 1200 r/min are shown in Figure 6. Figure 6 shows that all poles are placed on the left-hand side. This ensures that the first condition for system stability is satisfied.

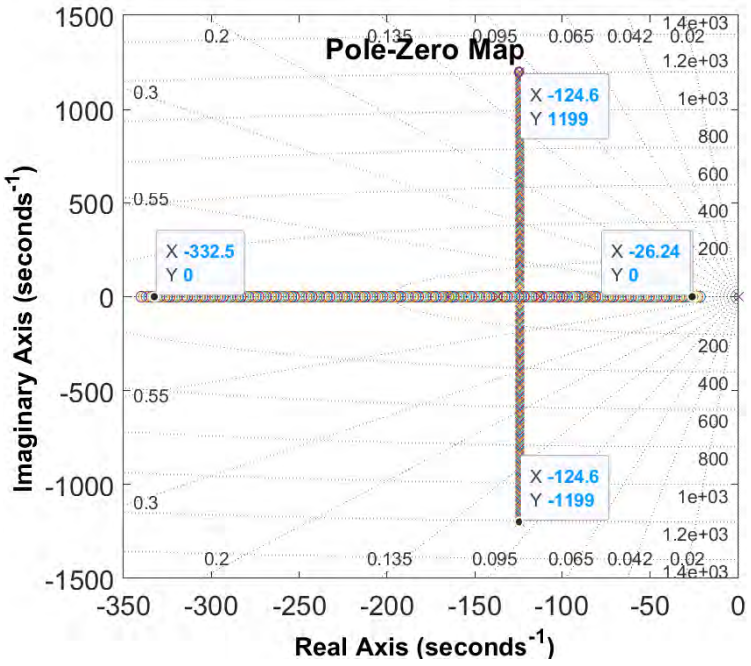


Figure 6. Poles of feed–forward linear transfer matrix G(s).

Second, the nonlinear feedback system satisfies Popov's integral inequality [39]. The nonlinear feedback model employing Popov's integral inequality is expressed as follows:

$$\eta(0, t_0) = \int_0^{t_0} e^T \mathbf{W} dt \geq -\gamma_0^2, \tag{34}$$

where $t_0 \geq 0$, and γ_0 is a constant gain with a positive real value that is independent of t_0. By the conventional form of the adaptive rule, the PI-based adaptive rule is expressed as:

$$\hat{\omega_r} = \int_0^t F_1(t)dt + F_2(t) + \hat{\omega_r}(0). \tag{35}$$

Substituting the value of **W**, Equation (34) becomes

$$\eta(0, t_0) = \int_0^{t_0} [e_d \frac{L_q}{L_d}(i_q) + [e_q(-i_d \frac{L_d}{L_q} - \frac{\lambda_m}{L_q})]]\Delta\omega_r dt \geq -\gamma_0^2. \tag{36}$$

By utilizing (35), the system becomes

$$\begin{aligned} \eta(0, t_0) = \int_0^{t_0} [[e_d \frac{L_q}{L_d}(i_q) + [e_q(-i_d \frac{L_d}{L_q} - \frac{\lambda_m}{L_q})]], \\ [\int_0^t F_1(t)dt + F_2(t) + \hat{\omega}_r(0) - \omega_r]]dt \geq -\gamma_0^2. \end{aligned} \tag{37}$$

The above equation is divided into two parts for simplification and is expressed as

$$\eta_{11}(0,t_0) = \int_0^{t_0} [[e_d \frac{L_q}{L_d}(i_q) + [e_q(-i_d \frac{L_d}{L_q} - \frac{\lambda_m}{L_q})]], \\ [\int_0^{t_0} F_1(t) + \hat{\omega}_r(0) - \omega_r]]dt \geq -\gamma_{11}^2, \tag{38}$$

and

$$\eta_{12}(0,t_0) = \int_0^{t_0} [[e_d \frac{L_q}{L_d}(i_q) + [e_q(-i_d \frac{L_d}{L_q} - \frac{\lambda_m}{L_q})]], \\ [F_2(t)]]dt \geq -\gamma_{12}^2, \tag{39}$$

where $\eta(0,t_0) = \eta_{11}(0,t_0) + \eta_{12}(0,t_0)$. The above-mentioned inequality solution is obtained by employing the Landau relationship [40].

$$\int_0^{t_0} kF(t)\frac{dF(t)}{dt} = \frac{k}{2}[F_{t_0}^2 - F_0^2] \geq \frac{-k}{2} f_{(0)}^2 \\ (k > 0). \tag{40}$$

From (40), the estimated rotor shaft speed ensure the following laws [39]:

$$\frac{dF(t)}{dt} = [e_d \frac{L_q}{L_d}(i_q) + [e_q(-i_d \frac{L_d}{L_q} - \frac{\lambda_m}{L_q})]], \tag{41}$$

and

$$kF(t) = [\int_0^{t_0} F_1(t)dt + \hat{\omega}_r(0) - \omega_r]. \tag{42}$$

By taking the derivative of (42) we obtain

$$k\frac{dF(t)}{dt} = F_1(t). \tag{43}$$

And, from (41), we derive $F_1(t)$ as

$$F_1(t) = k_1[e_d \frac{L_q}{L_d}(i_q) + [e_q(-i_d \frac{L_d}{L_q} - \frac{\lambda_m}{L_q})]]. \tag{44}$$

Solving for $F_2(t)$ in a similar manner, we obtain

$$F_2(t) = k_2[e_d \frac{L_q}{L_d}(i_q) + [e_q(-i_d \frac{L_d}{L_q} - \frac{\lambda_m}{L_q})]]. \tag{45}$$

The inequation (37) is expressed in the form of a simplified adaptive rule by substituting (44) and (45) into (35). Here, k_1 and k_2 are positive gains. By employing Popov's theory, we obtain $\lim_{t\to\infty} = [\varepsilon(\infty)]^T = 0$. Thus, adaptive rule (35) for estimating the rotor shaft speed based on the adaptive mechanism is asymptotically stable. The drive reference, adjustable model, and their errors are used to derive the estimated rotor shaft speed by employing the adaptive rule (35). Finally, the adaptive rule in terms of the proportional integral controller is derived as

$$\hat{\omega}_r = \hat{\omega}_r(0) + K_i \int_0^t [e_d \frac{L_q}{L_d}(i_q) + [e_q(-i_d \frac{L_d}{L_q} - \frac{\lambda_m}{L_q})]]dt + K_p[e_d \frac{L_q}{L_d}(i_q) + [e_q(-i_d \frac{L_d}{L_q} - \frac{\lambda_m}{L_q})]], \tag{46}$$

where K_p and K_i the estimated rotor shaft speed proportional-integral gain values, and $\hat{\omega}_r(0)$ is the initial estimated rotor shaft speed. The rotor shaft position is obtained by integrating the estimated rotor shaft speed as follows:

$$\hat{\theta}_r = \int_0^t \hat{\omega}_r dt \tag{47}$$

Stability Analysis

To verify the robustness of the MRAS-based self-sensing speed estimator, it is necessary to linearize the drive stator equation for marginal deflections for a definite steady-state solution. For a closed-loop system function, the pole-placement scheme is employed to analyze the stability of the MRAS-based speed estimator. Figure 7 shows a closed-loop structural diagram of the speed estimator. The closed-loop feed-forward transfer function for $G_F(\hat{\omega}_r)$ is derived by follows [39]:

$$\left.\frac{\Delta\epsilon}{\Delta\omega_r}\right|_{\omega_r^{ref}=0} = G_{F_{\hat{\omega}_r}} = \frac{[\frac{\lambda_m}{L_q}]^2\left(s+\frac{r_s}{L_d}\right)+\frac{\lambda_m}{L_q}i_q\hat{\omega}_r}{s^2+s\left(\frac{r_s}{L_q}+\frac{r_s}{L_d}\right)+\frac{r_s^2}{L_dL_q}+(\hat{\omega}_r)^2} \tag{48}$$

The transfer function of the PI controller in the speed-estimator model is expanded as follows:

$$G_{PI_{\hat{\omega}_r}} = K_{p\hat{\omega}_r} + \frac{K_{i\hat{\omega}_r}}{s} \tag{49}$$

$$H(s) = \frac{G_{F_{\hat{\omega}_r}} G_{PI_{\hat{\omega}_r}}}{1 + G_{F_{\hat{\omega}_r}} G_{PI_{\hat{\omega}_r}}} \tag{50}$$

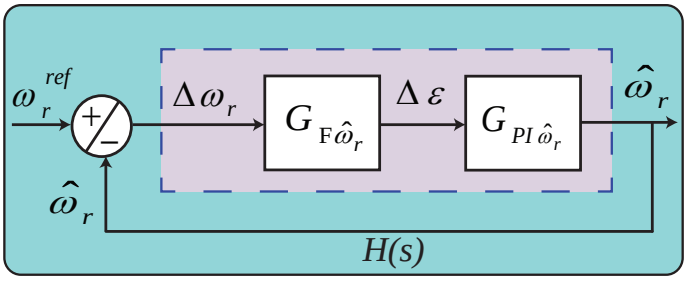


Figure 7. Structural diagram of MRAS speed estimation.

The control system dynamics for an MRAS-based self-sensing speed estimator block are illustrated by the closed-loop transfer function $H(s)$. The convergence of $\Delta\omega_r$ to zero is ensured by locating the poles of $H(s)$ at the origin of the s-plane. Figure 8 presents the pole-zero(pz) map for $H(s)$ in the speed range from -1200 to 1200 r/min. It is observed that all the poles are placed on the left-hand side of the s-plane, which presents a stable performance for different speed operating ranges. We observe that variations in the angular speed of the rotor do not affect the stability of the drive system.

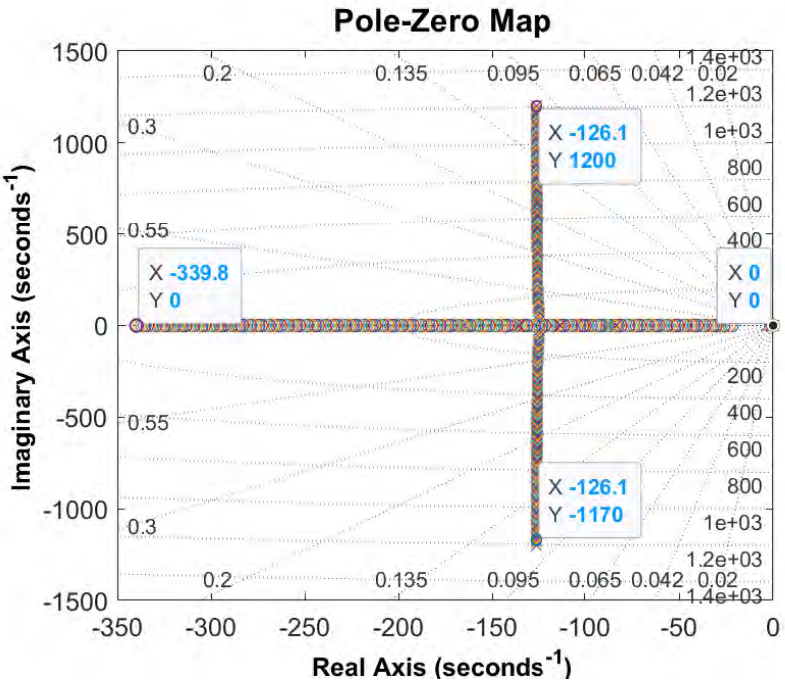


Figure 8. Poles of closed loop MRAS speed estimator $H(s)$.

4. Results and Discussion

A simulation model was developed for the self-sensing speed control of a motor drive with the proposed nonlinear cascaded control structure as shown in Figure 9. A computer-based model was developed in MATLAB/Simulink to verify the proposed method and ensure the feasibility of attaining the desired dynamic response under variable load conditions by utilizing the nominal drive parameters shown in Table 1. Different test cases were investigated to evaluate the drive control performance of the proposed and conventional control designs (e.g., the step convergence response for the input reference speed and load torque step variation, and the sinusoidal speed reference convergence response with electrical parameter variations) as given in Table 4.

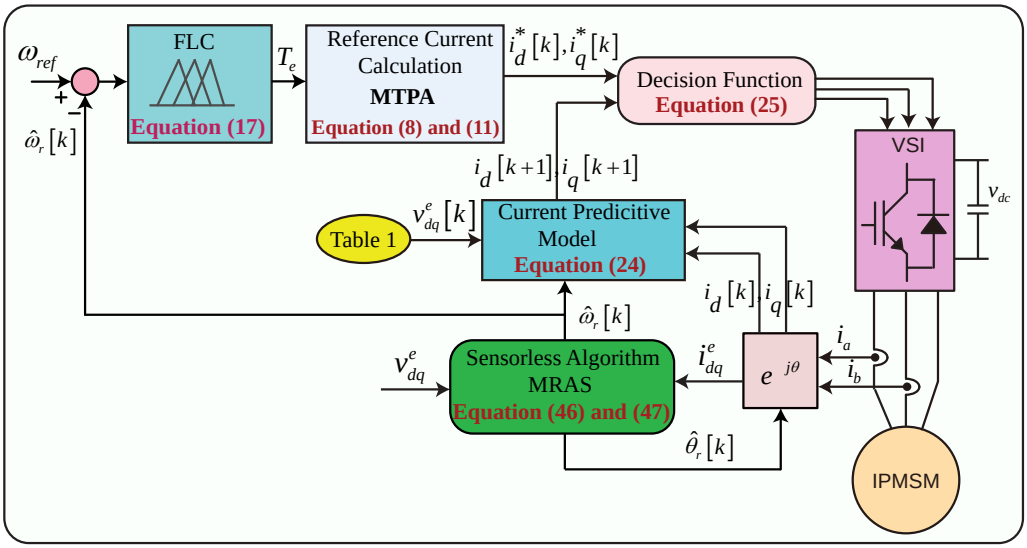


Figure 9. Simulation model nonlinear cascaded control structure with self-sensing algorithm.

Table 4. Case studies of drive response for different control design.

Case	Representation	Details	Parameter Values
1	Self-sensing speed convergence response with reference speed step variation	ω_r^{ref} = [0, 500, 600, 800, 700, −700, −330, 300] rpm at [0 0.09, 0.3, 0.5, 0.8, 1.2, 1.5, 1.7] s $T_L \rightarrow$ [3, 7] Nm at [0.7] s	Nominal
2	Self-sensing drive torque response with load step variation	T_L = [0, 3, 8, 11, 14, 5, 1] Nm at [0, 0.09, 0.2, 0.35, 0.55, 0.7, 0.85] s ω_r^{ref} = [800, −800] rpm at [0.5] s	Nominal
3	Self-sensing sinusoidal speed convergence response	$\omega_r^{ref} = 500\sin(20\pi t)$rpm	varied $r_s \uparrow 50\%$ $L_{dq} \uparrow 50\%$

Figure 10 shows the self-sensing speed performance for a wide range of speeds including low and reversal speeds under load variation at 0.7 s (i.e., Case 1) with the specified nominal drive parameters. Figure 11 reveals that the conventional cascaded control design has a speed overshoot with large settling times of 121.9 ms and 120.5 ms respectively. The load torque varies from 3.0 N.m to 7.0 N.m at 0.7 s and the performance analyses for the drive torque convergence rate and ripples at motor start-up, drive steady-state error, and steady-state speed ripple are observed. The proposed nonlinear cascaded control designs display less torque and speed ripples, a higher convergence rate, and a higher dynamic performance than those of conventional methods.

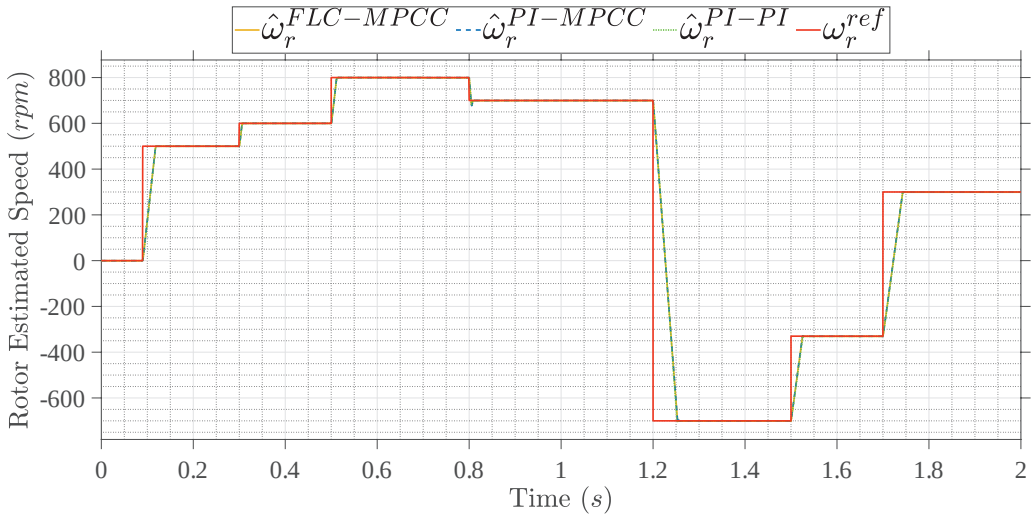


Figure 10. Response in the wide speed range for the positive and negative directions under abrupt load variation for the linear cascaded control design, eliminating linear cascaded control, and proposed nonlinear cascaded control design (Case 1).

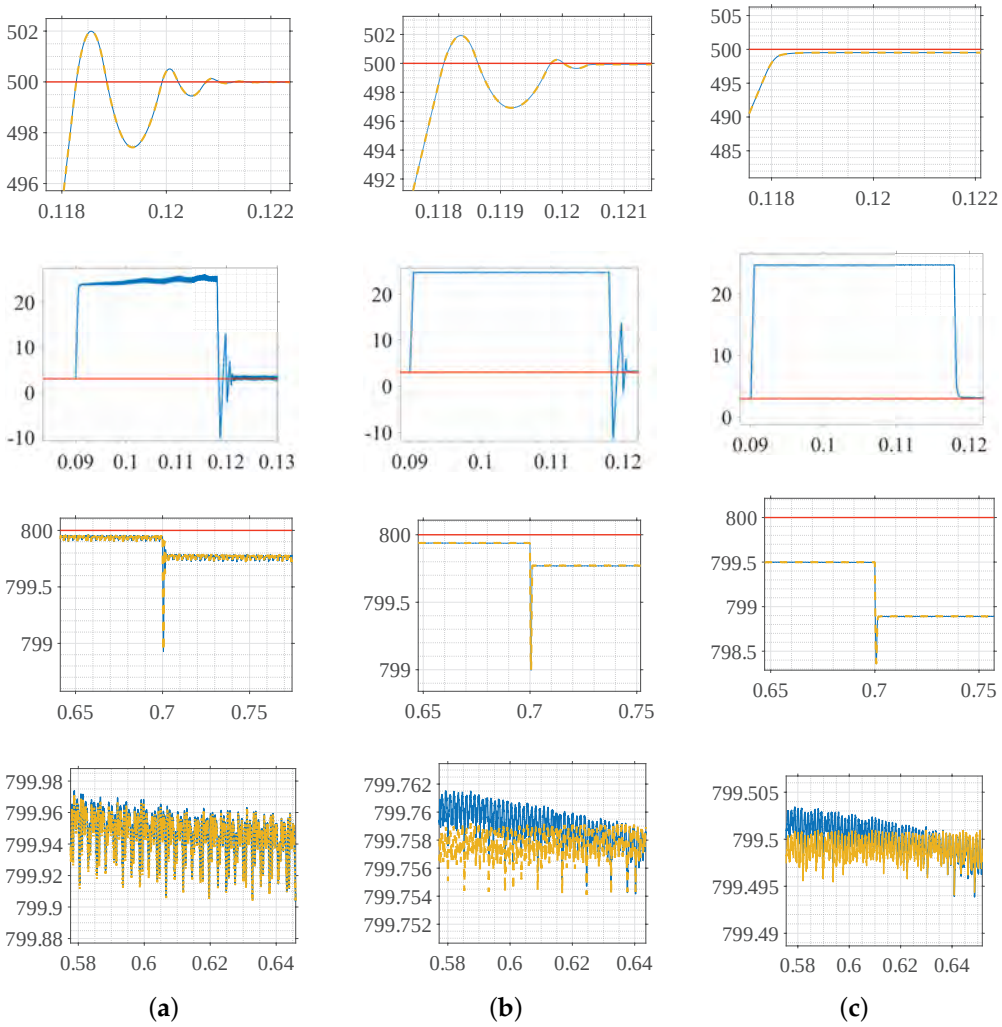


Figure 11. Expanded results of Figure 10. (**a**) Motor self–sensing speed response with conventional linear cascaded control design: speed overshoot, torque response, speed response with abrupt load variation, and steady–state speed ripples; (**b**) Motor self–sensing speed response with eliminating linear cascaded control design: speed overshoot, torque response, speed response with abrupt load variation, and steady–state speed ripples; (**c**) Motor self–sensing speed response with nonlinear cascaded control design: speed overshoot, torque response, speed response with abrupt load variation, and steady-state speed ripples.

Figure 12 shows the drive phase current, torque, and *dq*-axis current performance at the nominal speed, as specified in Figure 10. With the simplified MTPA control technique, the minimum current utilization for the maximum torque is observed in the proposed nonlinear cascaded control designs in conjunction with reduced current harmonics and torque ripples under abrupt load variations.

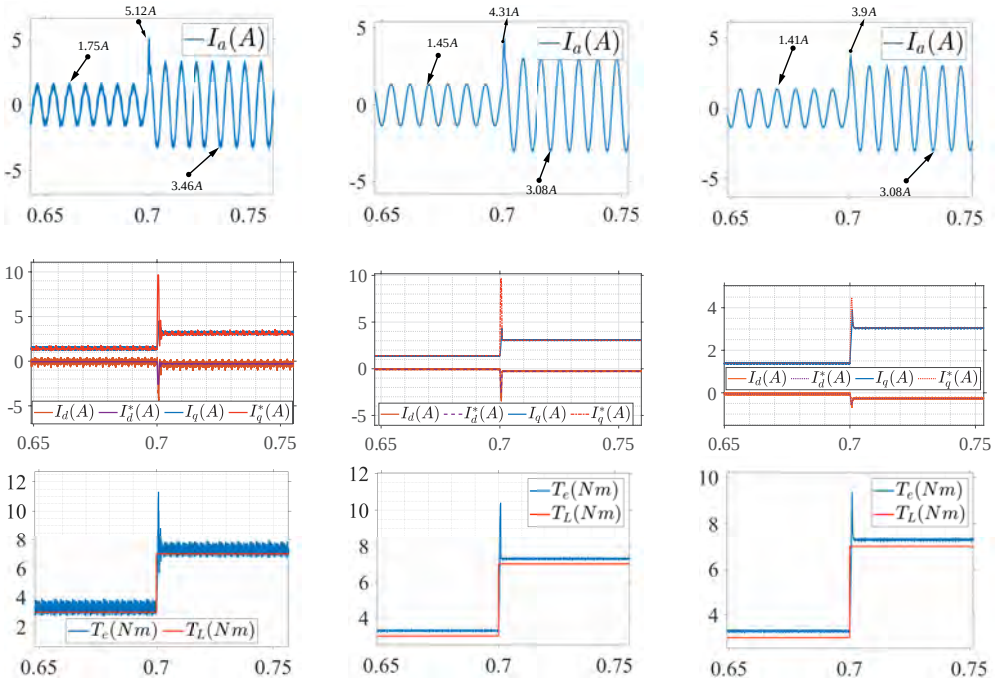


Figure 12. Motor current and torque response under nominal parameters with speed step variation. (**a**) Conventional linear cascaded control design with a PI controller for both speed and current regulation; (**b**) Eliminating a linear cascaded control design with a PI controller for speed regulation and MPCC for current regulation; (**c**) nonlinear cascaded control design with FLC for speed regulation and MPCC for current regulation.

Figure 13 depicts the harmonic distortion of the IPMSM phase current for different cascaded control designs. It is evident that the nonlinear cascaded control structure reduces the drive harmonic distortion and, in turn, enhances the drive performance. Figure 14 presents the drive dynamic performance under various load conditions at high and reverse speeds (i.e., Case 2). The nonlinear cascaded control design presents a better drive dynamic performance without undershoot for the speed response and the required minimum current for torque utilization with reduced harmonics. The remarkable *dq*-axis current response without overshoot under a load variation and the high torque convergence rate with reduced ripples demonstrate that the proposed control design is better than the conventional design.

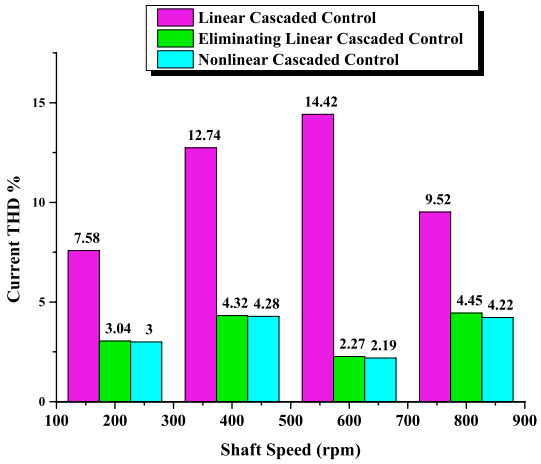


Figure 13. Phase current total harmonic distortion.

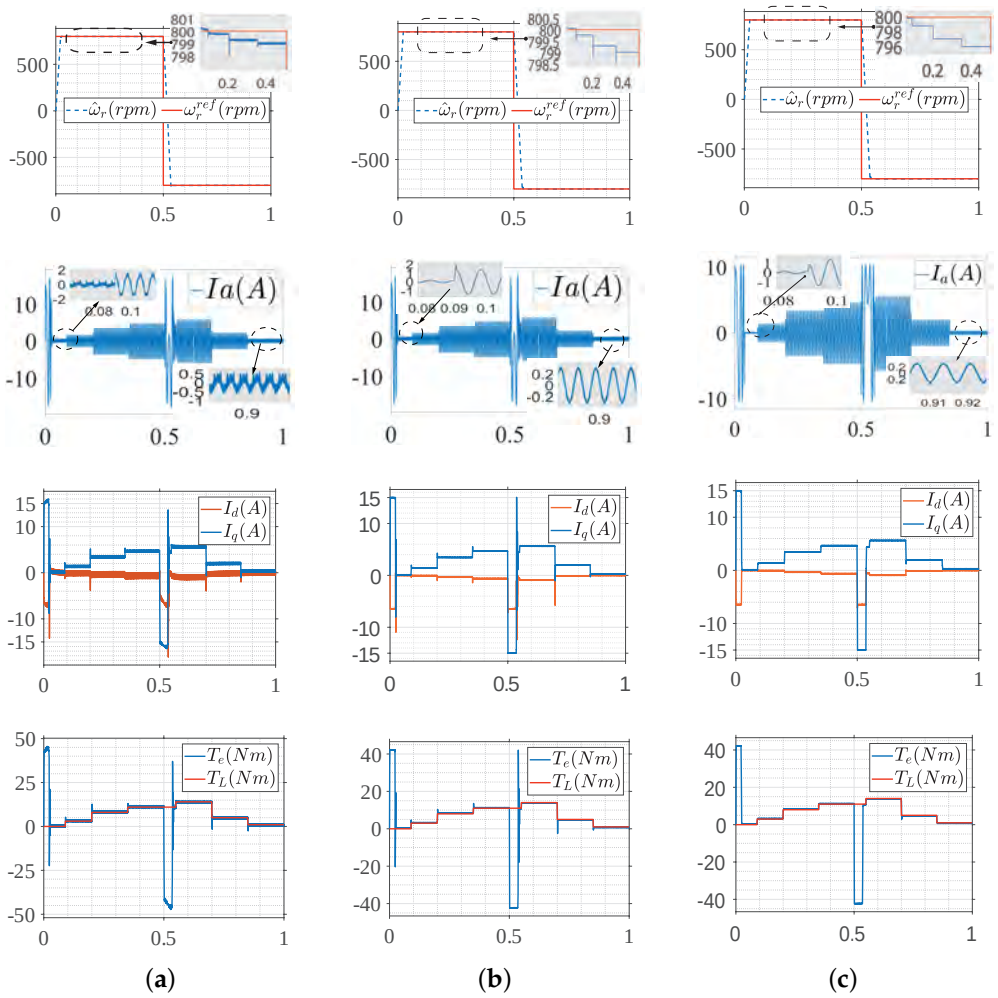


Figure 14. Motor current and torque response under nominal parameters with load step variation (Case 2). (**a**) Conventional linear cascaded control design with PI controller for both speed and current regulation; (**b**) Eliminating linear cascaded control design with PI controller for speed regulation and MPCC for current regulation; (**c**) nonlinear cascaded control design with FLC for speed regulation and MPCC for current regulation.

Figure 14 shows that the transient drive response of the proposed design is remarkable. It outperforms the conventional methods.

Figure 15 presents the simulation results for the conventional and proposed self-sensing control designs for a sinusoidal speed input reference under parameter variation (i.e., Case 3). The values of the motor parameters are varied in the IPMSM model and maintained constant in the predictive current control to ensure the robustness of the non-linear control and the performance of the IPMSM drive under parametric variation. It was observed that, under parameter variation, the self-sensing control design can accurately estimate the rotor shaft speed and position. The rotor shaft position error is minimized by employing non-linear cascaded control as compared to conventional control methods. The results show that the convergence under the proposed control design is superior to that of the conventional control method. Table 5 analyzes the drive performance of different cascaded control designs and shows the robustness of the proposed method.

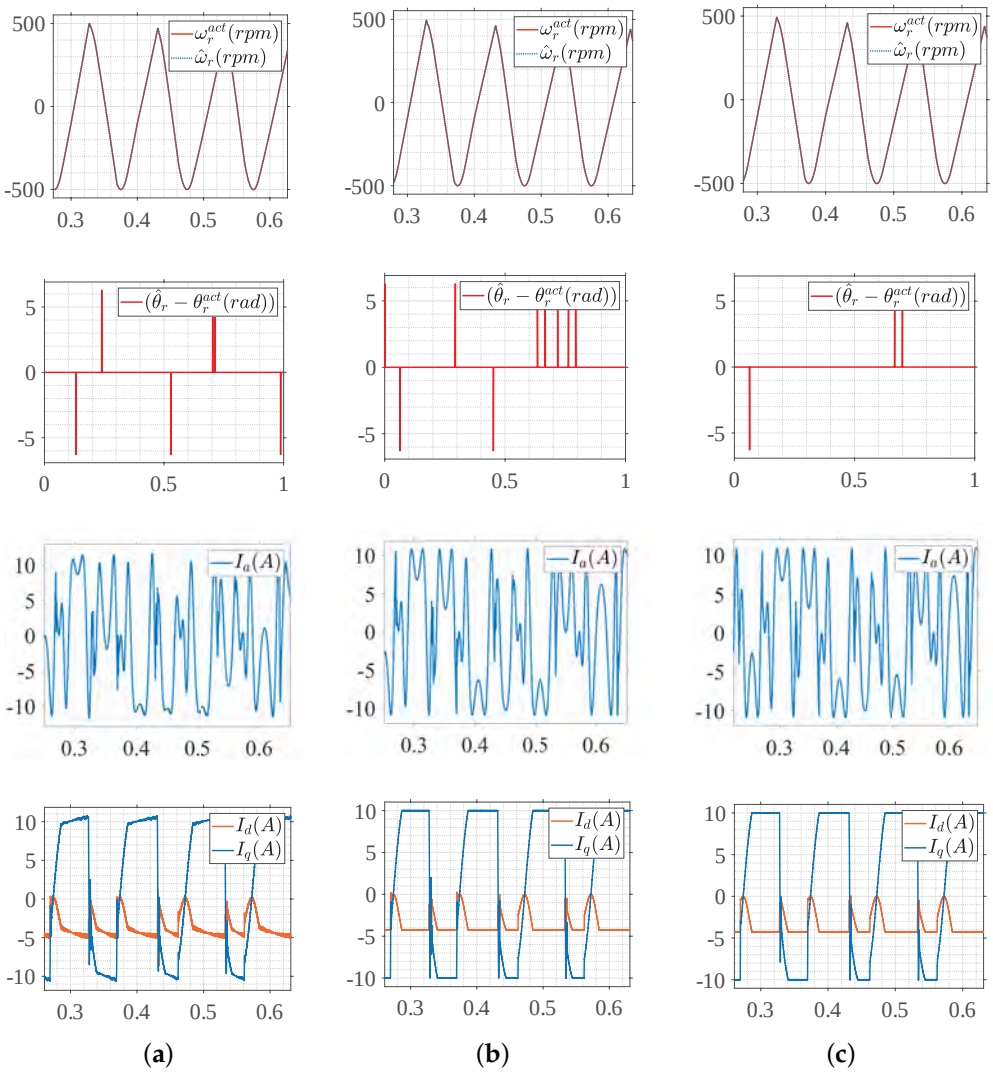


Figure 15. Motor drive response under parametric variation ($r_s \uparrow 50\,\%$ and $L_{dq} \uparrow 50\,\%$) and sinusoidal input (500 rpm at 10 Hz) (Case 3). (**a**) Motor self–sensing speed response with conventional linear cascaded control design: speed tracking, rotor position error, Phase–A current, and dq–axis currents; (**b**) Motor self–sensing speed response with elimination of linear cascaded control design: speed tracking, rotor position error, phase–A current, and dq–axis currents; (**c**) Motor self–sensing speed response with proposed nonlinear cascaded control design: speed tracking, rotor position error, Phase–A current, and dq–axis currents.

Table 5. Comparative analysis of system self-sensing performance by employing different cascaded control designs.

Parameters	PI-PI	PI-MPCC	FLC-MPCC
Dynamics	Good	Good	Remarkable
Speed Steady-state Error	Minimum	Moderate	Moderate
Speed Ripples	Larger	Moderate	Small
Speed Overshoot(%)	0.02	0.018	0.0
Speed Settling time(s)	0.1219	0.1205	0.118
Torque Response	Slow	Medium	Fast
Torque Ripple	Larger	Moderate	Small
Switching Frequency	Fixed	Variable	Variable
Current Harmonics	Higher	Moderate	Lower
Control Efficiency	Average	Good	Remarkable

5. Conclusions

A nonlinear cascade control structure with a self-sensing speed control design was investigated and implemented in this study. The motor drive dynamic performance, torque ripples, and current harmonics are significant issues that occur during transient and load variations. Moreover, at standstill, the drive displays a steady-state error that reveals an ineffective steady-state response. To overcome these issues, a control structure based on the FLC and FSCPC with an MRAS-based speed estimator is proposed. The proposed speed controller utilizes the estimated speed from the MRAS to improve the drive performance and achieve adequate accuracy under dynamic and standstill conditions over a wide speed operation range. The MRAS utilizes the current drive model and current estimation model and displays robustness over a wide speed range under various load conditions. In this study, a simple nonlinear expression for the *dq* reference current was incorporated in the motor drive system with known motor parameters. The stability of the self-sensing scheme is verified numerically by Popov's integral inequality, and the transfer function for the speed estimator based on MRAS is defined. Different test cases were simulated to verify the feasibility of the proposed control design. The results show that the proposed nonlinear cascaded control design with the MRAS-based speed estimation algorithm achieves better self-sensing speed control performance with a higher convergence rate and more rapid dynamic response than the conventional cascaded control structure. In addition, the torque and speed ripples and harmonic distortion of the phase current are reduced in the proposed method compared with those in traditional methods. The results indicate that the nonlinear cascaded control structure increases the robustness and steady-state performance of the drive.

Author Contributions: M.U. designed the proposed control, performed the simulation and analysed the results. The writing of original draft preparation was realized by M.U. J.K. reviewed, edit and supervised the work. All authors have read and agreed to the published version of the manuscript.

Funding: This study was supported by research funding from Chosun University, 2018.

Conflicts of Interest: The authors declare no conflict of interest.

References

1. Nam, K. Permanent Magnet AC Motors. In *AC Motor Control and Electric Vehicle Applications*; CRC Press: New York, NY, USA, 2010; Volume 1, pp. 133–158.
2. Boldea, I. Control issues in adjustable speed drives. *IEEE Ind. Electron. Mag.* **2008**, *2*, 32–50. [CrossRef]
3. Tursini, M.; Parasiliti, F.; Daqing, Z. Real-time gain tuning of PI controllers for high-performance PMSM drives. *IEEE Trans. Ind. Appl.* **2002**, *38*, 1018–1026. [CrossRef]
4. Zhang, G.; Furusho, J. Speed control of two-inertia system by PI/PID control. In Proceedings of the IEEE International Conference on Power Electronics and Drive Systems, Hong Kong, China, 27–29 July 1999; Volume 1, pp. 567–572. [CrossRef]
5. Yang, J.; Chen, W.; Li, S.; Guo, L.; Yan, Y. Disturbance/Uncertainty Estimation and Attenuation Techniques in PMSM Drives—A Survey. *IEEE Trans. Ind. Electron.* **2017**, *64*, 3273–3285. [CrossRef]
6. Domínguez, J.R.; Navarrete, A.; Meza, M.A.; Loukianov, A.G.; Cañedo, J. Digital sliding-mode sensorless control for surface-mounted PMSM. *IEEE Trans. Ind. Inform.* **2014**, *10*, 137–151. [CrossRef]
7. Zhang, X.; Sun, L.; Zhao, K.; Sun, L. Nonlinear speed control for PMSM system using sliding-mode control and disturbance compensation techniques. *IEEE Trans. Ind. Electron.* **2013**, *28*, 1358–1365. [CrossRef]
8. Underwood, S.J.; Husain, I. Online parameter estimation and adaptive control of permanent-magnet synchronous machines. *IEEE Trans. Ind. Electron.* **2010**, *57*, 2435–2443. [CrossRef]
9. Li, S.; Liu, Z. Adaptive speed control for permanent-magnet synchronous motor system with variations of load inertia. *IEEE Trans. Ind. Electron.* **2009**, *56*, 3050–3059. [CrossRef]
10. El-Sousy, F.F.M. Hybrid H^{∞}-based wavelet-neural-network tracking control for permanent-magnet synchronous motor servo drives. *IEEE Trans. Ind. Electron.* **2010**, *57*, 3157–3166. [CrossRef]
11. El-Sousy, F.F.M. Intelligent optimal recurrent wavelet elman neural network control system for permanent-magnet synchronous motor servo drive. *IEEE Trans. Ind. Inform.* **2013**, *9*, 1986–2003. [CrossRef]
12. Camacho, E.F.; Bordons, C. *Model Predictive Control*; Springer: London, UK, 2007.
13. Rawlings, J.B.; Mayne, D.Q. *Model Predictive Control: Theory and Design*; Nob Hill: Madison, WI, USA, 2009.
14. Qin, S.J.; Badgwell, T.A. A survey of industrial model predictive control technology. *Control Eng. Pract.* **2003**, *11*, 733–764. [CrossRef]

15. Cortes, P.; Kazmierkowski, M.P.; Kennel, R.M.; Quevedo, D.E.; Rodriguez, J. Predictive control in power electronics and drives. *IEEE Trans. Ind. Electron.* **2008**, *55*, 4312–4324. [CrossRef]
16. Malesani, L.; Mattavelli, P.; Buso, S. Robust dead-beat current control for PWM rectifiers and active filters. *IEEE Trans. Ind. Appl.* **1999**, *35*, 613–620. [CrossRef]
17. Usama, M.; Jaehong, K. Simplified model predicted current control method for speed control of non-silent permanent magnet synchronous motors. In Proceedings of the 2020 3rd International Conference on Computing, Mathematics and Engineering Technologies (iCoMET), Sukkur, Pakistan, 29–30 January 2020; pp. 1–5. [CrossRef]
18. Fuentes, E.J.; Silva, C.A.; Yuz, J.I. Predictive speed control of a two-mass system driven by a permanent magnet synchronous motor. *IEEE Trans. Ind. Electron.* **2012**, *59*, 2840–2848. [CrossRef]
19. Preindl, M.; Bolognani, S. Model predictive direct speed control with finite control set of PMSM drive systems. *IEEE Trans. Ind. Electron.* **2013**, *28*, 1007–1015. [CrossRef]
20. Errouissi, R.; Ouhrouche, M.; Chen, W.; Trzynadlowski, A.M. Robust cascaded nonlinear predictive control of a permanent magnet synchronous motor with antiwindup compensator. *IEEE Trans. Ind. Electron.* **2012**, *59*, 3078–3088. [CrossRef]
21. Lu, P. Optimal predictive control of continuous non-linear systems. *Int. J. Control* **1995**, *62*, 633–649. [CrossRef]
22. Chen, W.-H.; Ballance, D.J.; Gawthrop, P.J. Optimal control of non-linear systems: A predictive control approach. *Automatica* **2003**, *39*, 633–641. [CrossRef]
23. Chen, W.; Ballance, D.J.; Gawthrop, P.J.; Gribble, J.J.; O'Reilly, J. Non-linear PID predictive controller. *Control Theory Appl.* **1999**, *146*, 603–611.:19990744. [CrossRef]
24. Maiti, S.; Chakraborty, C.; Sengupta, S. Simulation studies on model reference adaptive controller based speed estimation technique for the vector controlled permanent magnet synchronous motor drive. *Simul. Model. Pract. Theory* **2009**, *17*, 585–596. [CrossRef]
25. An, Q.; Sun, L. Online parameter identification for vector controlled PMSM drives using adaptive algorithm. In Proceedings of the IEEE Vehicle Power and Propulsion Conference, Harbin, China, 3–5 September 2008; pp. 1–6. [CrossRef]
26. Rashed, M.; MacConnell, P.F.A.; Stronach, A.F.; Acarnley, P. Sensorless indirect-rotor-field-orientation speed control of a permanent-magnet synchronous motor with stator-resistance estimation. *IEEE Trans. Ind. Electron.* **2007**, *54*, 1664–1675. [CrossRef]
27. Usama, M.; Kim, J. Robust adaptive observer-based finite control set model predictive current control for sensorless speed control of surface permanent magnet synchronous motor. *Trans. Inst. Meas. Control* **2021**. [CrossRef]
28. Liang, Y.; Li, Y. Sensorless control of PM synchronous motors based on MRAS method and initial position estimation. In Proceedings of the Sixth International Conference on Electrical Machines and Systems, Beijing, China, 9–11 November 2003; Volume 1, pp. 96–99.
29. Morimoto, S.; Sanada, M.; Takeda, Y. Wide-speed operation of interior permanent magnet synchronous motors with high-performance current regulator. *IEEE Trans. Ind. Appl.* **1994**, *30*, 920–926. [CrossRef]
30. Sun, T.; Wang, J.; Chen, X. Maximum torque per ampere (MTPA) control for interior permanent magnet synchronous machine drives based on virtual signal injection. *IEEE Trans. Power Electron.* **2015**, *30*, 5036–5045. [CrossRef]
31. Butt, C.B.; Hoque, M.A.; Rahman, M.A. Simplified fuzzy-logic-based MTPA speed control of IPMSM drive. *IEEE Trans. Ind. Appl.* **2004**, *40*, 1529–1535. [CrossRef]
32. Rodriguez, J.; Pontt, J.; Silva, C.A.; Correa, P.; Lezana, P.; Cortes, P. Predictive current control of a voltage source inverter. *IEEE Trans. Ind. Electron.* **2007**, *54*, 495–503. [CrossRef]
33. Hossain, M.J.; Hoque, M.A.; Islam, K.K. Simplified fuzzy control for flux-weakening speed control of IPMSM drive. *Adv. Fuzzy Syst.* **2011**, *9*. [CrossRef]
34. Emami, M.R.; Turksen, I.B.; Goldenberg, A.A. Development of a systematic methodology of fuzzy logic modeling. *IEEE Trans. Fuzzy Syst.* **1998**, *6*, 346–361. [CrossRef]
35. Azam, M.H.; Hasan, M.H.; Hassan, S.; Abdulkadir, S.J. Fuzzy type-1 triangular membership function approximation using fuzzy C-means. In Proceedings of the 2020 International Conference on Computational Intelligence (ICCI), Bandar Seri Iskandar, Malaysia, 8–9 October 2020; pp. 115–120. [CrossRef]
36. Uddin, N.N.; Rahman, M.A. High-speed control of IPMSM drives using improved fuzzy logic algorithms. *IEEE Trans. Ind. Electron.* **2007**, *54*, 190–199. [CrossRef]
37. Usama, M; Kim, J. Performance improvement speed control of IPMSM drive based on nonlinear current control. *Turk. J. Electr. Eng. Comput. Sci.* **2021**, in press. [CrossRef]
38. Astrom, K.; Wittenmark, B. *Model Refernece Adaptive Systems in Adaptive Control*; Dover Publications: Mineola, NY, USA, 2008; pp. 185–255.
39. Khlaief, A.; Boussak, M.; Chaari, A. A MRAS-based stator resistance and speed estimation for sensorless vector controlled IPMSM drive. *Electr. Power Syst. Res.* **2014**, *108*, 1–15. [CrossRef]
40. Landau, I. A hyperstability criterion for model reference adaptive control systems. *IEEE Trans. Automat. Contr.* **1969**, *14*, 552–555. [CrossRef]